

# Search for Cosmic-Ray Events Using Radio Signals and CNNs in Data from the IceTop Enhancement Prototype Station

## The IceCube Collaboration

(a complete list of authors can be found at the end of the proceedings)

*E-mail:* [arehman@udel.edu](mailto:arehman@udel.edu), [alan.coleman@physics.uu.se](mailto:alan.coleman@physics.uu.se), [fgs@udel.edu](mailto:fgs@udel.edu),  
[danakull@udel.edu](mailto:danakull@udel.edu)

Cosmic-ray air showers emit radio waves that can be used to measure the properties of cosmic-ray primary particles. The radio detection technique presents several advantages, such as low cost and year-round duty cycle as well as the ability to provide high sensitivity to  $X_{\max}$  and energy estimation with minimal theoretical uncertainties, making it a promising tool for studying cosmic rays at the highest energies. However, the primary limitation of radio detection is the irreducible background from various sources that obscure the impulsive signals generated by air showers. To address this issue, we investigated the use of Convolutional Neural Networks (CNNs), trained on CoREAS simulations and radio backgrounds measured by a prototype station at the South Pole. We developed two different CNNs: a *Classifier* that distinguishes between cosmic ray event radio signals and pure background waveforms, and a *Denoiser* that mitigates background noise to recover the underlying cosmic-ray signal. After training the networks we apply them to the air-shower data to search for radio events. With two months data, we were able to identify 51 candidate events. The event's arrival direction reconstructed using CNN denoised radio waveforms is found to be in good agreement with the IceTop reconstruction. Finally, our approach demonstrated improved directional reconstruction compared to traditional methods.

**Corresponding authors:** Abdul Rehman<sup>1\*</sup>, Alan Coleman<sup>2</sup>, Frank G. Schröder<sup>1,3</sup>, Dana Kullgren<sup>1</sup>

<sup>1</sup> *Bartol Research Institute, Department of Physics and Astronomy, University of Delaware, Newark, DE, 19716, USA*

<sup>2</sup> *Department of Physics and Astronomy, Uppsala University, Uppsala SE-752 37, Sweden*

<sup>3</sup> *Karlsruhe Institute of Technology, Institute for Astroparticle Physics, 76021 Karlsruhe, Germany*

\* Presenter

The 38th International Cosmic Ray Conference (ICRC2023)  
26 July – 3 August, 2023  
Nagoya, Japan



## 1. Introduction

Radio waves emitted during the development of cosmic-ray induced air showers exhibit impulsive and highly coherent characteristics. Primarily, this emission arises from the deflection of charged particles (mainly electrons and positrons) under the influence of the Lorentz force in Earth's magnetic field. This emission occurs within a frequency range spanning from a few megahertz (MHz) to a few gigahertz (GHz) in proximity to the Cherenkov ring. Radio experiments have successfully detected and utilized these air shower radio signals to improve the estimation of various properties, such as the energy of air showers and depth of the shower maximum,  $X_{\max}$  [1, 2]. In addition, radio detection offers additional advantages, including cost-effective instrumentation and a full-year duty cycle. Because of that, radio technique is being increasingly recognized for its potential in future cosmic-ray and neutrino experiments such as the second generation of the IceCube neutrino observatory, known as IceCube-Gen2 [3, 4]. Moreover, radio techniques are also being considered for enhancing current experiments, as exemplified by the proposed enhancement of the surface detector of IceCube, also known as IceTop [5]. This enhancement involves the integration of scintillator panels and radio antennas. The motivation behind this enhancement plan is to address the loss of sensitivity of IceTop caused by snow accumulation on top of the detectors [6]. Furthermore, this will also improve sky coverage and allow for the simultaneous measurement of different components of air showers [7].

Despite the numerous advantages of the radio detection technique, there are outstanding challenges due to continuous background noise from galactic and extragalactic sources, in addition to anthropogenic noise. These factors introduce interference with the air-shower signals, making it difficult to distinguish between signal and background. To address this issue, we have employed machine learning techniques, particularly convolutional neural networks (CNNs). The CNNs have already been used previously by [8, 9] for this purpose. We have also used them in our previous work and showed that the CNNs can successfully distinguish and denoise the air-shower signals, hence improving the accuracy of the event pulse time and power within the signal [10, 11].

### 1.1 Prototype station of IceTop Enhancement

To assess the efficacy and design of the proposed surface enhancement array, a prototype station was constructed in January 2020, within the footprint of IceTop, serving as a valuable test-bed [12]. Subsequently, the prototype station underwent hardware upgrades, including the replacement of scintillator panels and the adoption of a new data acquisition system (known as TAXI). Comprising 8 scintillator panels and 3 radio antennas, the prototype station successfully recorded air shower signals with both detection technologies [13]. Efforts are underway to deploy additional stations in the forthcoming seasons [14].

### 1.2 Data from the prototype station

For now, the data collected from the scintillators and antennas is obtained independently of the IceCube data acquisition system. These data streams are then transmitted separately to the north, where they are merged together using timestamp information, provided by the shared synchronization clock at the Pole. Each radio antenna has two channels (two polarization) that record waveforms independently at a sampling rate of 1 GSa/s. The read-out of cosmic-ray signals

in antennas is triggered by the scintillators, which require at least 6 out of 8 scintillators to register a hit within one microsecond [12]. Additionally, pure background waveforms are recorded when there is no scintillator trigger, with radio waveforms being periodically read out at a fixed rate ( $\sim 1/\text{min}$ ). These background waveforms, known as soft-triggered data, are used in studying the background at the pole and training the neural networks. For the foreground, joint events containing scintillator, radio, and IceTop data are formed when there is an overlap in the time of the scintillator and IceTop hits.

### 1.3 Architecture and Training of CNNs

The network architectures utilized in this study are based on our previous work, with slight modifications in the *Classifier*. For detailed information regarding the specific architectural details, please refer to [10, 11]. The Tensorflow [15] and Keras [16] libraries of Python are employed to create two distinct networks: the *Classifier* and the *Denoiser*. The construction of these networks involves utilizing 1D convolutional layers paired with max-pooling and up-sampling layers to form encoding and decoding layers, respectively.

During our testing and evaluation phase, an interesting observation emerged regarding the role of the encoding and decoding layers, contrary to our earlier work. Specifically, we found that incorporating the decoding layers did not yield significant improvements in the performance of the *Classifier* network. This observation led us to infer that the training process primarily occurs within the encoding layers, which are responsible for learning discriminative features from the input data. As a result, for the *Classifier* network, we exclusively utilize the encoding layers with an additional flattening and one-neuron dense layer at the end. Each convolution layer uses ReLU whereas the dense layer uses Sigmoid as the activation function. The output of the *Classifier* ranges between 0 and 1, with values close to zero indicating background-like input and values close to 1 indicating signal-like input.

In contrast, the *Denoiser* comprises both encoding and decoding layers, with a convolutional layer serving as the final layer to ensure that the output waveform retains the same shape as the input waveform. A linear activation function is employed in the final layer of *Denoiser*. Through testing, it was determined that three encoding layers yield the optimal results for the *Classifier*, as increasing the number of layers does not provide significant improvements. For the *Denoiser*, three pairs of encoding and decoding layers are used.

The data utilized for training and testing the networks is generated using CoREAS Monte Carlo simulations [17], which generate radio signals stemming from cosmic-ray air showers. Additionally, pure background data from the prototype station is used as noise samples. The simulated signals are combined with the background waveforms and the resulting waveforms are subsequently used to train the networks with the pure signals serving as labels for the *Denoiser*. For details on the processing of the data see [10, 11].

## 2. CNN implementation and Output

After the training phase, the networks are implemented within the radio component of the analysis framework developed by the IceCube Collaboration, known as IceTray [18]. Similar to the preprocessing applied to the training data, the scintillator-triggered radio waveforms are first

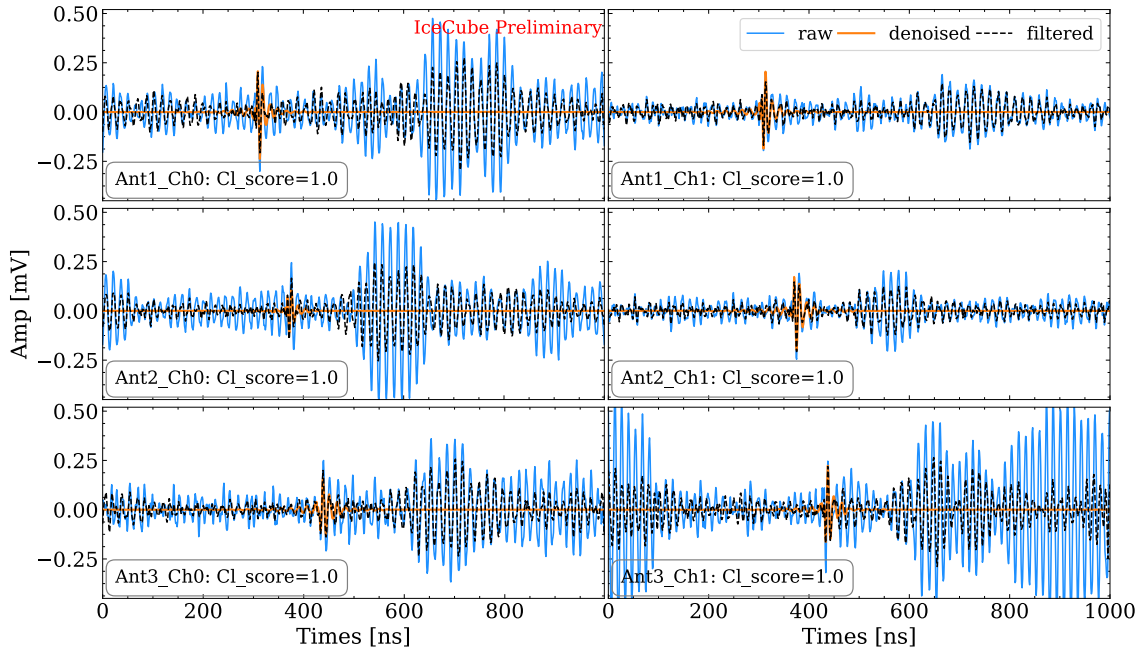


**Figure 1:** The figure displays the measured waveforms for all six channels from the three antennas. The raw waveforms, utilized as input for the networks, are depicted by solid blue lines. The cleaned waveforms, obtained through the denoising process, are presented in solid orange color. Additionally, the waveforms after applying the spike filter [19] are shown as black dashed lines. The output of the *Classifier*, represented as the *Cl\_score*, is displayed as text for each of the six channels.

processed to remove certain read-out artifacts. After that, all the electronic responses (e.g., the Low Noise Amplifier (LNA) and cable attenuation) are removed from these waveforms. Subsequently, the waveforms from each antenna undergo processing through their respectively trained CNN. The resulting output includes the computation of a *Classifier* score (*Cl\_score*) for each channel trace, and removing the noise from the waveform is done using the *Denoiser* network. Figure 1 provides an illustrative example, where the recorded waveforms from the antennas, after some pre-processing, are depicted by blue solid lines. These waveforms serve as the input for the networks. The denoised traces are represented by the orange solid line, while the corresponding *Cl\_score* is provided as text for each channel waveform. From the figure, it can be seen that all six channels receive the maximum *Classifier* score and the *Denoiser* successfully eliminates the background from the waveforms. Additionally, the figure also displays the filtered traces (dashed black color), which are obtained by applying a spike filter to the raw (blue-colored) waveforms (for detailed information on the spike filter, refer to [19]).

## 2.1 Quality Cuts

In the specific example illustrated in fig. 1, a best-case scenario is depicted. However, such optimal outcomes are not always observed. Therefore, to filter out the poorly reconstructed events, we developed a set of quality cuts. To derive the cuts, we applied both networks on pure background waveform (soft-triggered data). The results are presented in fig. 2 (left). The y-axis represents the *Classifier* score for the traces, while the denoised maximum amplitude, which corresponds to the

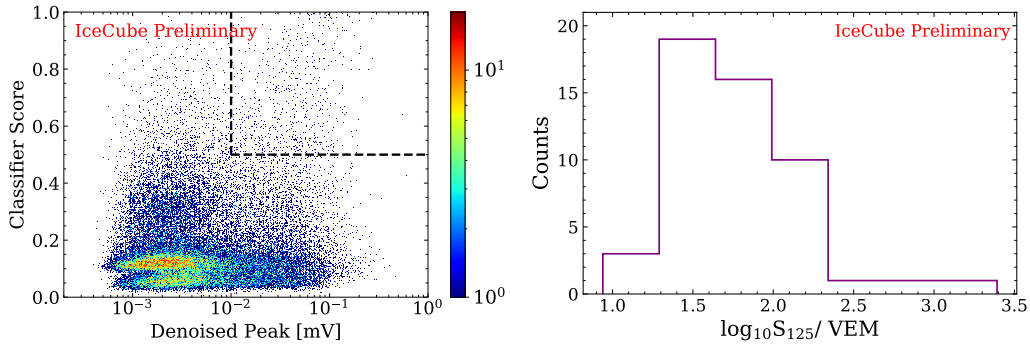


**Figure 2:** Left: the quality cuts employed for event filtering are depicted. The y-axis represents the *Classifier* score, while the x-axis represents the peak amplitude of the denoised waveforms. The allowed values for both quantities are represented by the black dashed box. Right: distribution of  $\log_{10}S_{125}$  (used as the energy proxy for IceTop) of all the events that pass the quality cuts.

maximum instantaneous amplitude computed from the denoised traces, is plotted on the x-axis. To achieve a 99% rejection rate of background events, a simplified threshold-based cut is employed. Specifically, in order to identify traces with a radio signal, we have chosen threshold values of *Classifier* score  $\geq 0.5$  and denoised maximum amplitude  $\geq 0.01$  mV.

## 2.2 Reconstruction of events

To reconstruct the arrival direction of air shower events, we use the denoised waveforms. For each antenna, we select the channel with the greater maximum amplitude to derive the arrival time in each antenna. The direction is then estimated via fitting a shower front model given by a plane moving at the speed of light. The fit is done using a weighted Chi-sq where the weights are taken to be the maximum amplitude of the denoised pulse. For IceTop reconstruction, we use the standard energy and arrival direction reconstruction [20]. Note that the angular resolution of IceTop for energies above 10 PeV (and thus relevant for this study) is less than one degree.

## 3. Results

We analyzed a two-month dataset encompassing January and February of 2022 in search of radio events. In addition to the quality cuts described earlier in section 2.1, we imposed an additional criterion that the radio-reconstructed arrival direction must be within five degrees of the standard IceTop reconstruction.

After applying all these quality cuts, we successfully identified 51 events during our search period ( $\approx 1$  / day). As an energy estimator we use the standard value of  $\log_{10}S_{125}$ , the expected signal in the station at a lateral distance of 125 m from the shower's axis. This value is linear with energy to within a few percent. The distribution of  $\log_{10}S_{125}$  values for the 51 events is depicted on the right in fig. 2. For scale,  $\log_{10}S_{125} = 2$  corresponds to  $\approx 100$  PeV primary energy of the air shower. However, it should be noted that this energy estimation is a first-order approximation in our case, as this parameter is primarily optimized for small zenith angles where IceTop exhibits its highest sensitivity whereas most of our events lie in the higher zenith angle range.

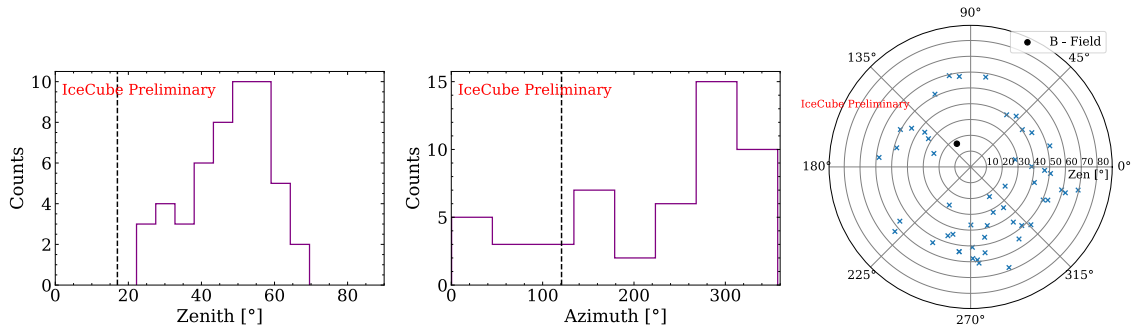


**Figure 3:** The distribution of arrival directions for all the radio events successfully passed the quality cuts. Left: Zenith angle distribution indicating that the majority of events are concentrated in the higher zenith range. Middle: Azimuth distribution of radio events. Right: Polar representation of the arrival direction of events.

The zenith and azimuth angle distributions of radio events are shown in fig. 3. The black-filled circle on the polar (right) plot and the dashed lines on the other plots corresponds to the Earth's magnetic field. At the South Pole, this corresponds to a direction approximately  $18^\circ$  from the zenith and  $30^\circ$  degrees west of grid-north. From the left panel, it can be noted that the majority of the identified radio events are concentrated in the large zenith angle range, with a decreasing trend as the angles surpass 60 degrees. This can be attributed to the radio read-out triggering mechanism, which relies on the scintillators. At large zenith angles ( $\geq 65^\circ$ ), the efficiency of the scintillators decreases significantly, leading to a reduced detection rate at those values. Additionally, we also require event coincidence with the IceTop, which also exhibits decreased sensitivity at higher zenith angles. Furthermore, no event  $< 20$  degrees can also be attributed to the near-vertical magnetic field present at the pole.

Even with very small statistics, looking at the azimuth, fig. 3 middle, and polar, fig. 3 right, plots we observe an increase in event counts in the direction opposite to the geomagnetic field. This finding aligns with our expectations, as the primary source of radio emission from cosmic rays stems from the geomagnetic emission resulting from the Lorentz force [21].

### 3.1 Core Positions of radio events

The core positions of all the events were also reconstructed using the information from IceTop. In fig. 4, left, the core locations reconstructed using IceTop are denoted by blue dots. The antenna locations are represented by black "X" marks, while the grey dots indicate the locations of the IceTop detectors (IceTop tanks). This plot shows that showers with core positions more than 400 meters away from the antennas were also detected. This is possible for more inclined showers due to two geometric effects. With increasing zenith angle, the location of  $X_{\max}$  is further away from the array due to the increased slant depth. The beamed cone thus has more geometric distance over which to spread out from the shower axis. Simultaneously, the *projected* size of the footprint scales like  $\sec(\theta)$ . Indeed in the right panel of fig. 4 we see that the events furthest from the array are also the most inclined.

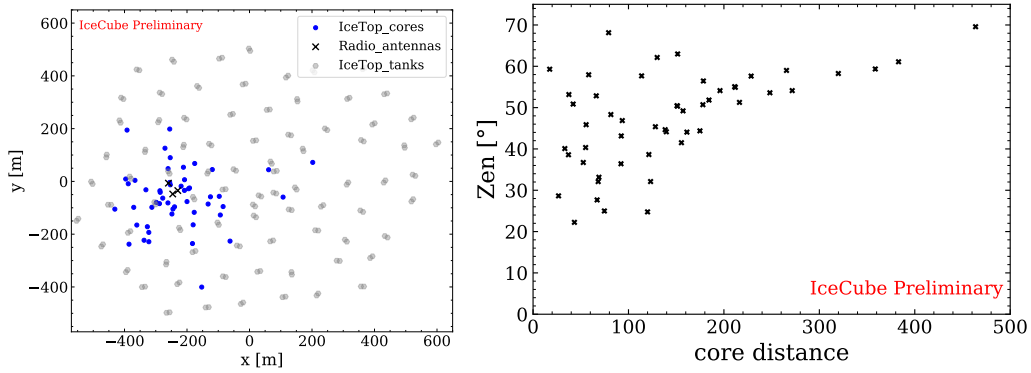


**Figure 4:** Left: the IceTop reconstructed core locations for all the events. The blue dots represent the core positions, while the black "X" marks indicate the locations of the three antennas. The grey dots represent the locations of the IceTop tanks (detectors). Right: The plot shows the distance of the core position from the center of the antennas as a function of the corresponding zenith angle for each event.

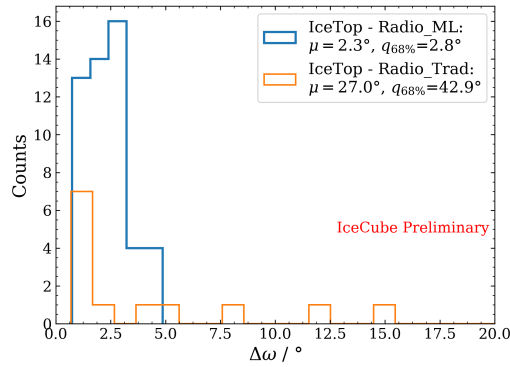


**Figure 5:** The angular deviation of the radio reconstructed arrival direction from the IceTop is shown. The blue distribution represents the 51 events that passed the quality cuts and utilized the denoised waveforms for arrival direction reconstruction. The orange distribution on the other hand represents the subset of 13 events (out of the 51) where reconstruction was performed using the filtered waveform, shown in fig. 1. All remaining events in the sample lie on the right side of the distribution, not displayed in the figure.

### 3.2 Comparison with Traditional methods

Finally, we conducted a preliminary comparison with the traditional method used for the search of radio events. We selected the 51 events that passed our defined quality cuts and processed them through the traditional analysis chain [13]. This involved taking the raw waveforms (shown in blue in fig. 1) and applying a frequency weighting [19] to obtain filtered waveforms. The arrival direction was then reconstructed using these filtered waveforms and compared with the IceTop reconstruction. In fig. 5, the total angular deviation from the IceTop reconstruction is shown for both the waveforms processed by the CNN (shown in blue) and the filtered waveforms (shown in orange). To provide a clearer view, the plot is zoomed-in along the x-axis. The orange distribution includes only 13 out of the 51 events within the plotted range, while the remaining events extend further towards the right of the distribution. This comparison, however, is preliminary and a more comprehensive analysis is the topic for the future. These results, nevertheless, already show promising improvements from the traditional methods.

#### 4. Conclusion and Outlook

Presented in this work are the preliminary results of our study to search for cosmic-ray air showers using radio waveforms, which have been classified and denoised using convolutional neural networks (CNNs). The CNNs were trained on background waveforms obtained from the prototype station of the IceTop enhancement station and subsequently applied to cosmic-ray radio waveforms triggered by the scintillators. During a two-month search period in 2022, a total of 51 air-shower events with radio signals were identified. The reconstructed arrival directions, obtained by utilizing CNN denoised waveforms, were compared to the standard IceTop reconstruction and exhibited good agreement. Furthermore, we conducted a simple comparative test with traditional methods, which showed promising improvements when employing CNNs. This outcome aligns with our earlier findings, demonstrating that the denoising of pulses through CNNs effectively reduces pulse time uncertainty in each antenna. Further improvements in CNN performance can be achieved by utilizing preprocessed data for training purposes and integrating information from the two channels of antennas.

#### References

- [1] F. G. Schröder *Progress in Particle and Nuclear Physics* **93** (Mar., 2017) 1–68.
- [2] T. Huege *Phys. Rept.* **620** (2016) 1–52.
- [3] **IceCube** Collaboration, A. Coleman *PoS ICRC2023* (these proceedings) 205.
- [4] **IceCube-Gen2** Collaboration, F. G. Schröder *PoS* **424** (2023) 058.
- [5] **IceCube** Collaboration, M. G. Aartsen *et al.* *JINST* **12** no. 03, (2017) P03012.
- [6] K. Rawlins *PoS ICRC2015* (2016) 628.
- [7] A. Haungs *EPJ Web Conf.* **210** (2019) 06009.
- [8] D. Shipilov *et al.* *EPJ Web Conf.* **216** (2019) 02003.
- [9] M. Erdmann, F. Schlüter, and R. Smida *JINST* **14** no. 04, (2019) P04005.
- [10] A. Rehman, A. Coleman, F. G. Schröder, and D. Kostunin *PoS ICRC2021* (2021) 417.
- [11] **IceCube** Collaboration, A. Rehman *PoS ARENA2022* (2022) 012.
- [12] **IceCube** Collaboration, R. Abbasi *et al.* *PoS ICRC2021* (2021) 225.
- [13] **IceCube** Collaboration, R. Abbasi *et al.* *PoS ICRC2021* (2021) 314.
- [14] **IceCube** Collaboration, S. Shefali *PoS ICRC2023* (these proceedings) 342.
- [15] M. Abadi *et al.* *arXiv:1603.04467* (2016) .
- [16] F. Chollet *et al.*, “Keras.” <https://keras.io>, 2015.
- [17] T. Huege, M. Ludwig, and C. W. James *AIP Conference Proceedings* **1535** (2013) 128–132.
- [18] **IceCube** Collaboration, R. Abbasi *et al.* *JINST* **17** no. 06, (2022) P06026.
- [19] **IceCube** Collaboration, R. Abbasi *et al.* *PoS ICRC2021* (2021) 317.
- [20] **IceCube** Collaboration, K. Rawlins *Phys. Atom. Nucl.* **83** no. 2, (2020) 280–284.
- [21] E. N. Paudel, A. Coleman, and F. G. Schroeder *Phys. Rev. D* **105** no. 10, (2022) 103006.

## Full Author List: IceCube Collaboration

R. Abbasi<sup>17</sup>, M. Ackermann<sup>63</sup>, J. Adams<sup>18</sup>, S. K. Agarwalla<sup>40, 64</sup>, J. A. Aguilar<sup>12</sup>, M. Ahlers<sup>22</sup>, J.M. Alameddine<sup>23</sup>, N. M. Amin<sup>44</sup>, K. Andeen<sup>42</sup>, G. Anton<sup>26</sup>, C. Argüelles<sup>14</sup>, Y. Ashida<sup>53</sup>, S. Athanasiadou<sup>63</sup>, S. N. Axani<sup>44</sup>, X. Bai<sup>50</sup>, A. Balagopal V.<sup>40</sup>, M. Baricevic<sup>40</sup>, S. W. Barwick<sup>30</sup>, V. Basu<sup>40</sup>, R. Bay<sup>8</sup>, J. J. Beatty<sup>20, 21</sup>, J. Becker Tjus<sup>11, 65</sup>, J. Beise<sup>61</sup>, C. Bellenghi<sup>27</sup>, C. Benning<sup>1</sup>, S. BenZvi<sup>52</sup>, D. Berley<sup>19</sup>, E. Bernardini<sup>48</sup>, D. Z. Besson<sup>36</sup>, E. Blaufuss<sup>19</sup>, S. Blot<sup>63</sup>, F. Bontempo<sup>31</sup>, J. Y. Book<sup>14</sup>, C. Boscolo Meneguolo<sup>48</sup>, S. Böser<sup>41</sup>, O. Botner<sup>61</sup>, J. Böttcher<sup>1</sup>, E. Bourbeau<sup>22</sup>, J. Braun<sup>40</sup>, B. Brinson<sup>6</sup>, J. Brostean-Kaiser<sup>63</sup>, R. T. Burley<sup>2</sup>, R. S. Busse<sup>43</sup>, D. Butterfield<sup>40</sup>, M. A. Campana<sup>49</sup>, K. Carloni<sup>14</sup>, E. G. Carnie-Bronca<sup>2</sup>, S. Chattopadhyay<sup>40, 64</sup>, N. Chau<sup>12</sup>, C. Chen<sup>6</sup>, Z. Chen<sup>55</sup>, D. Chirkin<sup>40</sup>, S. Choi<sup>56</sup>, B. A. Clark<sup>19</sup>, L. Classen<sup>43</sup>, A. Coleman<sup>61</sup>, G. H. Collin<sup>15</sup>, A. Connolly<sup>20, 21</sup>, J. M. Conrad<sup>15</sup>, P. Coppin<sup>13</sup>, P. Correa<sup>13</sup>, D. F. Cowen<sup>59, 60</sup>, P. Dave<sup>6</sup>, C. De Clercq<sup>13</sup>, J. J. DeLaunay<sup>58</sup>, D. Delgado<sup>14</sup>, S. Deng<sup>1</sup>, K. Deoskar<sup>54</sup>, A. Desai<sup>40</sup>, P. Desati<sup>40</sup>, K. D. de Vries<sup>13</sup>, G. de Wasseige<sup>37</sup>, T. DeYoung<sup>24</sup>, A. Diaz<sup>15</sup>, J. C. Díaz-Vélez<sup>40</sup>, M. Dittmer<sup>43</sup>, A. Domi<sup>26</sup>, H. Dujmovic<sup>40</sup>, M. A. DuVernois<sup>40</sup>, T. Ehrhardt<sup>41</sup>, P. Eller<sup>27</sup>, E. Ellinger<sup>62</sup>, S. El Mentawi<sup>1</sup>, D. Elsässer<sup>23</sup>, R. Engel<sup>31, 32</sup>, H. Erpenbeck<sup>40</sup>, J. Evans<sup>19</sup>, P. A. Evenson<sup>44</sup>, K. L. Fan<sup>19</sup>, K. Fang<sup>40</sup>, K. Farrag<sup>16</sup>, A. R. Fazley<sup>7</sup>, A. Fedynitch<sup>57</sup>, N. Feigl<sup>10</sup>, S. Fiedlschuster<sup>26</sup>, C. Finley<sup>54</sup>, L. Fischer<sup>63</sup>, D. Fox<sup>59</sup>, A. Frankowiak<sup>11</sup>, A. Fritz<sup>41</sup>, P. Fürst<sup>1</sup>, J. Gallagher<sup>39</sup>, E. Ganster<sup>1</sup>, A. Garcia<sup>14</sup>, L. Gerhardt<sup>9</sup>, A. Ghadimi<sup>58</sup>, C. Glaser<sup>61</sup>, T. Glauch<sup>27</sup>, T. Glusenkamp<sup>26, 61</sup>, N. Goehke<sup>32</sup>, J. G. Gonzalez<sup>44</sup>, S. Goswami<sup>58</sup>, D. Grant<sup>24</sup>, S. J. Gray<sup>19</sup>, O. Gries<sup>1</sup>, S. Griffin<sup>40</sup>, S. Griswold<sup>52</sup>, K. M. Groth<sup>22</sup>, C. Günther<sup>1</sup>, P. Gutjahr<sup>23</sup>, C. Haack<sup>26</sup>, A. Hallgren<sup>61</sup>, R. Halliday<sup>24</sup>, L. Halve<sup>1</sup>, F. Halzen<sup>40</sup>, H. Hamdaoui<sup>55</sup>, M. Ha Minh<sup>27</sup>, K. Hanson<sup>40</sup>, J. Hardin<sup>15</sup>, A. A. Harnisch<sup>24</sup>, P. Hatch<sup>33</sup>, A. Haungs<sup>31</sup>, K. Helbing<sup>62</sup>, J. Hellrung<sup>11</sup>, F. Henningsen<sup>27</sup>, L. Heuermann<sup>1</sup>, N. Heyer<sup>61</sup>, S. Hickford<sup>62</sup>, A. Hidvegi<sup>54</sup>, C. Hill<sup>16</sup>, G. C. Hill<sup>2</sup>, K. D. Hoffman<sup>19</sup>, S. Hori<sup>40</sup>, K. Hoshina<sup>40, 66</sup>, W. Hou<sup>31</sup>, T. Huber<sup>31</sup>, K. Hultqvist<sup>54</sup>, M. Hünnefeld<sup>23</sup>, R. Hussain<sup>40</sup>, K. Hymon<sup>23</sup>, S. In<sup>56</sup>, A. Ishihara<sup>16</sup>, M. Jacquart<sup>40</sup>, O. Janik<sup>1</sup>, M. Jansson<sup>54</sup>, G. S. Japaridze<sup>5</sup>, M. Jeong<sup>56</sup>, M. Jin<sup>14</sup>, B. J. P. Jones<sup>4</sup>, D. Kang<sup>31</sup>, W. Kang<sup>56</sup>, X. Kang<sup>49</sup>, A. Kappes<sup>43</sup>, D. Kappesser<sup>41</sup>, L. Kardum<sup>23</sup>, T. Karg<sup>63</sup>, M. Karl<sup>27</sup>, A. Karle<sup>40</sup>, U. Katz<sup>26</sup>, M. Kauer<sup>40</sup>, J. L. Kelley<sup>40</sup>, A. Khatee Zathul<sup>40</sup>, A. Kheirandish<sup>34, 35</sup>, J. Kiryluk<sup>55</sup>, S. R. Klein<sup>8, 9</sup>, A. Kochocki<sup>24</sup>, R. Koirala<sup>44</sup>, H. Kolanoski<sup>10</sup>, T. Kontrims<sup>27</sup>, L. Köpke<sup>41</sup>, C. Kopper<sup>26</sup>, D. J. Koskinen<sup>22</sup>, P. Koundal<sup>31</sup>, M. Kovacevich<sup>49</sup>, M. Kowalski<sup>10, 63</sup>, T. Kozynets<sup>22</sup>, J. Krishnamoorthi<sup>40, 64</sup>, K. Kruiswijk<sup>37</sup>, E. Krupczak<sup>24</sup>, D. Kullgren<sup>44</sup>, A. Kumar<sup>63</sup>, E. Kun<sup>11</sup>, N. Kurahashi<sup>49</sup>, N. Lad<sup>63</sup>, C. Lagunas Gualda<sup>63</sup>, M. Lamoureux<sup>37</sup>, M. J. Larson<sup>19</sup>, S. Latseva<sup>1</sup>, F. Lauber<sup>62</sup>, J. P. Lazar<sup>14, 40</sup>, J. W. Lee<sup>56</sup>, K. Leonard DeHolton<sup>60</sup>, A. Leszczyńska<sup>44</sup>, M. Lincetto<sup>11</sup>, Q. R. Liu<sup>40</sup>, M. Liubarska<sup>25</sup>, E. Lohfink<sup>41</sup>, C. Love<sup>49</sup>, C. J. Lozano Mariscal<sup>43</sup>, L. Lu<sup>40</sup>, F. Lucarelli<sup>28</sup>, W. Luszczyk<sup>20, 21</sup>, Y. Lyu<sup>8, 9</sup>, J. Madsen<sup>40</sup>, K. B. M. Mahn<sup>24</sup>, Y. Makino<sup>40</sup>, E. Manao<sup>27</sup>, S. Mancina<sup>40, 48</sup>, W. Marie Sainte<sup>40</sup>, I. C. Mariş<sup>12</sup>, S. Marka<sup>46</sup>, Z. Marka<sup>46</sup>, M. Marsee<sup>58</sup>, I. Martinez-Soler<sup>14</sup>, R. Maruyama<sup>45</sup>, F. Mayhew<sup>24</sup>, T. McElroy<sup>25</sup>, F. McNally<sup>38</sup>, J. V. Mead<sup>22</sup>, K. Meagher<sup>40</sup>, S. Mechbal<sup>63</sup>, A. Medina<sup>21</sup>, M. Meier<sup>16</sup>, Y. Merckx<sup>13</sup>, L. Merten<sup>11</sup>, J. Micallef<sup>24</sup>, J. Mitchell<sup>7</sup>, T. Montaruli<sup>28</sup>, R. W. Moore<sup>25</sup>, Y. Morii<sup>16</sup>, R. Morse<sup>40</sup>, M. Moulai<sup>40</sup>, T. Mukherjee<sup>31</sup>, R. Naab<sup>63</sup>, R. Nagai<sup>16</sup>, M. Nakos<sup>40</sup>, U. Naumann<sup>62</sup>, J. Necker<sup>63</sup>, A. Negi<sup>4</sup>, M. Neumann<sup>43</sup>, H. Niederhausen<sup>24</sup>, M. U. Nisa<sup>24</sup>, A. Noell<sup>1</sup>, A. Novikov<sup>44</sup>, S. C. Nowicki<sup>24</sup>, A. Obertacke Pollmann<sup>16</sup>, V. O'Dell<sup>40</sup>, M. Oehler<sup>31</sup>, B. Oeyen<sup>29</sup>, A. Olivas<sup>19</sup>, R. Ørsøe<sup>27</sup>, J. Osborn<sup>40</sup>, E. O'Sullivan<sup>61</sup>, H. Pandya<sup>44</sup>, N. Park<sup>33</sup>, G. K. Parker<sup>4</sup>, E. N. Paudel<sup>44</sup>, L. Paul<sup>42, 50</sup>, C. Pérez de los Heros<sup>61</sup>, J. Peterson<sup>40</sup>, S. Philippen<sup>1</sup>, A. Pizzuto<sup>40</sup>, M. Plum<sup>50</sup>, A. Pontén<sup>61</sup>, Y. Popovych<sup>41</sup>, M. Prado Rodriguez<sup>40</sup>, B. Pries<sup>24</sup>, R. Procter-Murphy<sup>19</sup>, G. T. Przybylski<sup>9</sup>, C. Raab<sup>37</sup>, J. Rack-Helleis<sup>41</sup>, K. Rawlins<sup>3</sup>, Z. Rechac<sup>40</sup>, A. Rehman<sup>44</sup>, P. Reichherzer<sup>11</sup>, G. Renzi<sup>12</sup>, E. Resconi<sup>27</sup>, S. Reusch<sup>63</sup>, W. Rhode<sup>23</sup>, B. Riedel<sup>40</sup>, A. Rifaie<sup>1</sup>, E. J. Roberts<sup>2</sup>, S. Robertson<sup>8, 9</sup>, S. Rodan<sup>56</sup>, G. Roellinghoff<sup>56</sup>, M. Rongen<sup>26</sup>, C. Rott<sup>53, 56</sup>, T. Ruhe<sup>23</sup>, L. Ruohan<sup>27</sup>, D. Ryckbosch<sup>29</sup>, I. Safa<sup>14, 40</sup>, J. Saffer<sup>32</sup>, D. Salazar-Gallegos<sup>24</sup>, P. Sampathkumar<sup>31</sup>, S. E. Sanchez Herrera<sup>24</sup>, A. Sandrock<sup>62</sup>, M. Santander<sup>58</sup>, S. Sarkar<sup>25</sup>, S. Sarkar<sup>47</sup>, J. Savelberg<sup>1</sup>, P. Savina<sup>40</sup>, M. Schaufel<sup>1</sup>, H. Schieler<sup>31</sup>, S. Schindler<sup>26</sup>, L. Schlickmann<sup>1</sup>, B. Schlüter<sup>43</sup>, F. Schlüter<sup>12</sup>, N. Schmeisser<sup>62</sup>, T. Schmidt<sup>19</sup>, J. Schneider<sup>26</sup>, F. G. Schröder<sup>31, 44</sup>, L. Schumacher<sup>26</sup>, G. Schwefer<sup>1</sup>, S. Sclafani<sup>19</sup>, D. Seckel<sup>44</sup>, M. Seikh<sup>36</sup>, S. Seunarine<sup>51</sup>, R. Shah<sup>49</sup>, A. Sharma<sup>61</sup>, S. Shefali<sup>32</sup>, N. Shimizu<sup>16</sup>, M. Silva<sup>40</sup>, B. Skrzypek<sup>14</sup>, B. Smithers<sup>4</sup>, R. Snihur<sup>40</sup>, J. Soedingrekso<sup>23</sup>, A. Sogaard<sup>22</sup>, D. Soldin<sup>32</sup>, P. Soldin<sup>1</sup>, G. Sommani<sup>11</sup>, C. Spannfellner<sup>27</sup>, G. M. Spiczak<sup>51</sup>, C. Spiering<sup>63</sup>, M. Stamatikos<sup>21</sup>, T. Stanev<sup>44</sup>, T. Stetzelberger<sup>9</sup>, T. Stürwald<sup>62</sup>, T. Stuttard<sup>22</sup>, G. W. Sullivan<sup>19</sup>, I. Taboada<sup>6</sup>, S. Ter-Antonyan<sup>7</sup>, M. Thiesmeyer<sup>1</sup>, W. G. Thompson<sup>14</sup>, J. Thwaites<sup>40</sup>, S. Tilav<sup>44</sup>, K. Tollefson<sup>24</sup>, C. Tönnis<sup>56</sup>, S. Toscano<sup>12</sup>, D. Tosi<sup>40</sup>, A. Trettin<sup>63</sup>, C. F. Tung<sup>6</sup>, R. Turcotte<sup>31</sup>, J. P. Twagirayezu<sup>24</sup>, B. Ty<sup>40</sup>, M. A. Unland Elorrieta<sup>43</sup>, A. K. Upadhyay<sup>40, 64</sup>, K. Upshaw<sup>7</sup>, N. Valtonen-Mattila<sup>61</sup>, J. Vandenbroucke<sup>40</sup>, N. van Eijndhoven<sup>13</sup>, D. Vannerom<sup>15</sup>, J. van Santen<sup>63</sup>, J. Vara<sup>43</sup>, J. Veitch-Michaelis<sup>40</sup>, M. Venugopal<sup>31</sup>, M. Vereecken<sup>37</sup>, S. Verpoest<sup>44</sup>, D. Veske<sup>46</sup>, A. Vijai<sup>19</sup>, C. Walck<sup>54</sup>, C. Weaver<sup>24</sup>, P. Weigel<sup>15</sup>, A. Weindl<sup>31</sup>, J. Weldert<sup>60</sup>, C. Wendt<sup>40</sup>, J. Werthebach<sup>23</sup>, M. Weyrauch<sup>31</sup>, N. Whitehorn<sup>24</sup>, C. H. Wiebusch<sup>1</sup>, N. Willey<sup>24</sup>, D. R. Williams<sup>58</sup>, L. Witthaus<sup>23</sup>, A. Wolf<sup>1</sup>, M. Wolf<sup>27</sup>, G. Wrede<sup>26</sup>, X. W. Xu<sup>7</sup>, J. P. Yanez<sup>25</sup>, E. Yildizci<sup>40</sup>, S. Yoshida<sup>16</sup>, R. Young<sup>36</sup>, F. Yu<sup>14</sup>, S. Yu<sup>24</sup>, T. Yuan<sup>40</sup>, Z. Zhang<sup>55</sup>, P. Zhelnin<sup>14</sup>, M. Zimmerman<sup>40</sup>

<sup>1</sup> III. Physikalisches Institut, RWTH Aachen University, D-52056 Aachen, Germany

<sup>2</sup> Department of Physics, University of Adelaide, Adelaide, 5005, Australia

<sup>3</sup> Dept. of Physics and Astronomy, University of Alaska Anchorage, 3211 Providence Dr., Anchorage, AK 99508, USA

<sup>4</sup> Dept. of Physics, University of Texas at Arlington, 502 Yates St., Science Hall Rm 108, Box 19059, Arlington, TX 76019, USA

<sup>5</sup> CTSPS, Clark-Atlanta University, Atlanta, GA 30314, USA

<sup>6</sup> School of Physics and Center for Relativistic Astrophysics, Georgia Institute of Technology, Atlanta, GA 30332, USA

<sup>7</sup> Dept. of Physics, Southern University, Baton Rouge, LA 70813, USA

<sup>8</sup> Dept. of Physics, University of California, Berkeley, CA 94720, USA

<sup>9</sup> Lawrence Berkeley National Laboratory, Berkeley, CA 94720, USA

<sup>10</sup> Institut für Physik, Humboldt-Universität zu Berlin, D-12489 Berlin, Germany

<sup>11</sup> Fakultät für Physik & Astronomie, Ruhr-Universität Bochum, D-44780 Bochum, Germany

<sup>12</sup> Université Libre de Bruxelles, Science Faculty CP230, B-1050 Brussels, Belgium

- <sup>13</sup> Vrije Universiteit Brussel (VUB), Dienst ELEM, B-1050 Brussels, Belgium  
<sup>14</sup> Department of Physics and Laboratory for Particle Physics and Cosmology, Harvard University, Cambridge, MA 02138, USA  
<sup>15</sup> Dept. of Physics, Massachusetts Institute of Technology, Cambridge, MA 02139, USA  
<sup>16</sup> Dept. of Physics and The International Center for Hadron Astrophysics, Chiba University, Chiba 263-8522, Japan  
<sup>17</sup> Department of Physics, Loyola University Chicago, Chicago, IL 60660, USA  
<sup>18</sup> Dept. of Physics and Astronomy, University of Canterbury, Private Bag 4800, Christchurch, New Zealand  
<sup>19</sup> Dept. of Physics, University of Maryland, College Park, MD 20742, USA  
<sup>20</sup> Dept. of Astronomy, Ohio State University, Columbus, OH 43210, USA  
<sup>21</sup> Dept. of Physics and Center for Cosmology and Astro-Particle Physics, Ohio State University, Columbus, OH 43210, USA  
<sup>22</sup> Niels Bohr Institute, University of Copenhagen, DK-2100 Copenhagen, Denmark  
<sup>23</sup> Dept. of Physics, TU Dortmund University, D-44221 Dortmund, Germany  
<sup>24</sup> Dept. of Physics and Astronomy, Michigan State University, East Lansing, MI 48824, USA  
<sup>25</sup> Dept. of Physics, University of Alberta, Edmonton, Alberta, Canada T6G 2E1  
<sup>26</sup> Erlangen Centre for Astroparticle Physics, Friedrich-Alexander-Universität Erlangen-Nürnberg, D-91058 Erlangen, Germany  
<sup>27</sup> Technical University of Munich, TUM School of Natural Sciences, Department of Physics, D-85748 Garching bei München, Germany  
<sup>28</sup> Département de physique nucléaire et corpusculaire, Université de Genève, CH-1211 Genève, Switzerland  
<sup>29</sup> Dept. of Physics and Astronomy, University of Gent, B-9000 Gent, Belgium  
<sup>30</sup> Dept. of Physics and Astronomy, University of California, Irvine, CA 92697, USA  
<sup>31</sup> Karlsruhe Institute of Technology, Institute for Astroparticle Physics, D-76021 Karlsruhe, Germany  
<sup>32</sup> Karlsruhe Institute of Technology, Institute of Experimental Particle Physics, D-76021 Karlsruhe, Germany  
<sup>33</sup> Dept. of Physics, Engineering Physics, and Astronomy, Queen's University, Kingston, ON K7L 3N6, Canada  
<sup>34</sup> Department of Physics & Astronomy, University of Nevada, Las Vegas, NV, 89154, USA  
<sup>35</sup> Nevada Center for Astrophysics, University of Nevada, Las Vegas, NV 89154, USA  
<sup>36</sup> Dept. of Physics and Astronomy, University of Kansas, Lawrence, KS 66045, USA  
<sup>37</sup> Centre for Cosmology, Particle Physics and Phenomenology - CP3, Université catholique de Louvain, Louvain-la-Neuve, Belgium  
<sup>38</sup> Department of Physics, Mercer University, Macon, GA 31207-0001, USA  
<sup>39</sup> Dept. of Astronomy, University of Wisconsin–Madison, Madison, WI 53706, USA  
<sup>40</sup> Dept. of Physics and Wisconsin IceCube Particle Astrophysics Center, University of Wisconsin–Madison, Madison, WI 53706, USA  
<sup>41</sup> Institute of Physics, University of Mainz, Staudinger Weg 7, D-55099 Mainz, Germany  
<sup>42</sup> Department of Physics, Marquette University, Milwaukee, WI, 53201, USA  
<sup>43</sup> Institut für Kernphysik, Westfälische Wilhelms-Universität Münster, D-48149 Münster, Germany  
<sup>44</sup> Bartol Research Institute and Dept. of Physics and Astronomy, University of Delaware, Newark, DE 19716, USA  
<sup>45</sup> Dept. of Physics, Yale University, New Haven, CT 06520, USA  
<sup>46</sup> Columbia Astrophysics and Nevis Laboratories, Columbia University, New York, NY 10027, USA  
<sup>47</sup> Dept. of Physics, University of Oxford, Parks Road, Oxford OX1 3PU, United Kingdom  
<sup>48</sup> Dipartimento di Fisica e Astronomia Galileo Galilei, Università Degli Studi di Padova, 35122 Padova PD, Italy  
<sup>49</sup> Dept. of Physics, Drexel University, 3141 Chestnut Street, Philadelphia, PA 19104, USA  
<sup>50</sup> Physics Department, South Dakota School of Mines and Technology, Rapid City, SD 57701, USA  
<sup>51</sup> Dept. of Physics, University of Wisconsin, River Falls, WI 54022, USA  
<sup>52</sup> Dept. of Physics and Astronomy, University of Rochester, Rochester, NY 14627, USA  
<sup>53</sup> Department of Physics and Astronomy, University of Utah, Salt Lake City, UT 84112, USA  
<sup>54</sup> Oskar Klein Centre and Dept. of Physics, Stockholm University, SE-10691 Stockholm, Sweden  
<sup>55</sup> Dept. of Physics and Astronomy, Stony Brook University, Stony Brook, NY 11794-3800, USA  
<sup>56</sup> Dept. of Physics, Sungkyunkwan University, Suwon 16419, Korea  
<sup>57</sup> Institute of Physics, Academia Sinica, Taipei, 11529, Taiwan  
<sup>58</sup> Dept. of Physics and Astronomy, University of Alabama, Tuscaloosa, AL 35487, USA  
<sup>59</sup> Dept. of Astronomy and Astrophysics, Pennsylvania State University, University Park, PA 16802, USA  
<sup>60</sup> Dept. of Physics, Pennsylvania State University, University Park, PA 16802, USA  
<sup>61</sup> Dept. of Physics and Astronomy, Uppsala University, Box 516, S-75120 Uppsala, Sweden  
<sup>62</sup> Dept. of Physics, University of Wuppertal, D-42119 Wuppertal, Germany  
<sup>63</sup> Deutsches Elektronen-Synchrotron DESY, Platanenallee 6, 15738 Zeuthen, Germany  
<sup>64</sup> Institute of Physics, Sachivalaya Marg, Sainik School Post, Bhubaneswar 751005, India  
<sup>65</sup> Department of Space, Earth and Environment, Chalmers University of Technology, 412 96 Gothenburg, Sweden  
<sup>66</sup> Earthquake Research Institute, University of Tokyo, Bunkyo, Tokyo 113-0032, Japan

## Acknowledgements

The authors gratefully acknowledge the support from the following agencies and institutions: USA – U.S. National Science Foundation-Office of Polar Programs, U.S. National Science Foundation-Physics Division, U.S. National Science Foundation-EPSCoR, Wisconsin Alumni Research Foundation, Center for High Throughput Computing (CHTC) at the University of Wisconsin–Madison, Open Science

Grid (OSG), Advanced Cyberinfrastructure Coordination Ecosystem: Services & Support (ACCESS), Frontera computing project at the Texas Advanced Computing Center, U.S. Department of Energy-National Energy Research Scientific Computing Center, Particle astrophysics research computing center at the University of Maryland, Institute for Cyber-Enabled Research at Michigan State University, and Astroparticle physics computational facility at Marquette University; Belgium – Funds for Scientific Research (FRS-FNRS and FWO), FWO Odysseus and Big Science programmes, and Belgian Federal Science Policy Office (Belspo); Germany – Bundesministerium für Bildung und Forschung (BMBF), Deutsche Forschungsgemeinschaft (DFG), Helmholtz Alliance for Astroparticle Physics (HAP), Initiative and Networking Fund of the Helmholtz Association, Deutsches Elektronen Synchrotron (DESY), and High Performance Computing cluster of the RWTH Aachen; Sweden – Swedish Research Council, Swedish Polar Research Secretariat, Swedish National Infrastructure for Computing (SNIC), and Knut and Alice Wallenberg Foundation; European Union – EGI Advanced Computing for research; Australia – Australian Research Council; Canada – Natural Sciences and Engineering Research Council of Canada, Calcul Québec, Compute Ontario, Canada Foundation for Innovation, WestGrid, and Compute Canada; Denmark – Villum Fonden, Carlsberg Foundation, and European Commission; New Zealand – Marsden Fund; Japan – Japan Society for Promotion of Science (JSPS) and Institute for Global Prominent Research (IGPR) of Chiba University; Korea – National Research Foundation of Korea (NRF); Switzerland – Swiss National Science Foundation (SNSF); United Kingdom – Department of Physics, University of Oxford.